Journal of Materials Chemistry A

PAPER

Mesoporous TiO_2 beads for high efficiency CdS/CdSe quantum dot co-sensitized solar cells

Cite this: *J. Mater. Chem. A*, 2014, **2**, 2517

Ru Zhou,[ab] Qifeng Zhang,[a] Evan Uchaker,[a] Jolin Lan,[a] Min Yin*[b] and Guozhong Cao*[a]

Received 31st August 2013
Accepted 22nd November 2013

DOI: 10.1039/c3ta13460a

www.rsc.org/MaterialsA

Mesoporous TiO_2 beads with a combined effective light scattering effect and large surface area were prepared and studied for quantum dot-sensitized solar cell (QDSC) application. The photoanode films were composed of submicrometer-sized beads consisting of packed TiO_2 nanocrystallites. A power conversion efficiency up to 4.05% has been achieved for a CdS/CdSe quantum dot (QD) co-sensitized solar cell, which was constructed with the mesoporous TiO_2 beads prepared with a two-step method, in which an optimal amount of ammonia was adopted to etch TiO_2 spheres and achieve the desired porosity of the beads for QD adsorption. The high conversion efficiency was ascribed to a combined effect of the mesoporous structure, light scattering ability and good electrical conduction capability of the beads. It has been found that larger pores can be created by adding more ammonia during the solvothermal treatment, leading to easy penetration of the QDs into the inner pores of the mesoporous beads. An excessive amount of ammonia would lead to a low specific surface area and decrease of light scattering capability of the films. Electrochemical impedance spectroscopy analysis revealed a retarded charge recombination for the mesoporous TiO_2 beads treated with ammonia in view of a decreased contact area of the beads with the electrolyte, reflected in the increase of both open circuit voltage and fill factor of the solar cells.

1. Introduction

Quantum dot-sensitized solar cells (QDSCs) as a derivative of dye-sensitized solar cells (DSCs) have attracted considerable attention and been regarded as a promising alternative to conventional solid-state semiconductor solar cells.[1–5] QDSCs are relatively cost-effective and easy to manufacture, and furthermore, compared to organic dyes, narrow band gap semiconductor QDs possess multiple extraordinary optical and electrical properties in terms of (1) the tunable band gap across a wide energy range, (2) strong light absorption, (3) high stability against oxidative deterioration, (4) high extinction coefficients, and (5) large intrinsic dipole moment facilitating charge separation.[6–10] A high theoretical photovoltaic conversion efficiency up to 44% in view of the multiple excitation generation (MEG) effect,[11] beyond the traditional Shockley and Queisser limit of 32% for semiconductor solar cells,[12,13] has encouraged people to develop QDSCs with the use of CdS,[14–16] CdSe,[17,18] CdTe,[19,20] PbS,[21,22] and Ag_2S QDs[23,24] as sensitizers for light harvesting. Furthermore, some co-sensitization systems, especially the combination of CdS and CdSe QDs, have also been widely studied.[2,9,10,25–27] However, the power conversion efficiency of these QDSCs, typically with the efficiency of 15%, still lags far behind ~12% of DSCs.[28,29] Obviously efforts are needed to get a better fundamental understanding so as to develop the materials and nano/micro-structures for the QDSCs to achieve high power conversion efficiency and explore the full potential of the QDSCs.

The photovoltaic properties of QDSCs are collective results of several processes in series: effective capture of photons, generation of electron–hole pairs, separation of electrons and holes at interfaces, and transport of electrons and holes. All the processes are accompanied by charge recombination, and thus the power conversion efficiency is closely dependent on the competition between the generation/transportation and recombination of photoexcited carriers.[29,30] One of the key issues in all solar cells is to increase carrier generation and inhibit charge recombination. One-dimensional nanostructures, such as nanowires, nanorods and nanotubes, can facilitate the rapid collection of photogenerated electrons, and thus reduce charge recombination in view of their direct electrical pathways.[9,31,32] However, the insufficient internal surface area of the one-dimensional nanostructures restricts the amount of QDs loaded, and thus leads to low power conversion efficiency. The photoanode, as a very important component of QDSCs, requires a mesoporous wide-band gap oxide semiconductor with a sufficient surface area for high sensitizer loading, which favors large amounts of electron–hole pair

[a]*Department of Materials Science and Engineering, University of Washington, Seattle, WA 98195, USA. E-mail: gzcao@u.washington.edu; Fax: +1 206 543 3100; Tel: +1 206 616 9084*

[b]*Department of Physics, University of Science and Technology of China, Hefei 230026, China*

generation under sunlight excitation. In addition, light scattering with large particles has proven to be an effective approach to increase the light-harvesting capability of the photoanode, as theoretically predicted by Usami,[33] Ferber and Luther,[34] and Rothenberger.[35] TiO_2 mesoporous nanocrystalline films have been extensively studied as the photoanodes for QDSCs and DSCs due to their high internal surface area which maximizes the adsorption of sensitizers.[2,26,36,37] However, typical nanosized TiO_2 particles ($\approx$20 nm) in the working electrode are very weak scatterers in the generation of light scattering because the size of the nanoparticles is far smaller than the wavelength of visible light, resulting in a significant portion of the light emitted on the photoanodes transmitting through the film without interacting with the sensitizer.[29,38] According to the Mie theory and Anderson localization of light,[39,40] resonant scattering of light is predicted to occur for spherical particles, when the particle size is comparable to the wavelength of incident light. A strong scattering effect would extend the distance that light travels within the photoanode film, provide the photons with more opportunities to be absorbed by the sensitizer (*i.e.*, dye molecules or QDs), and thus eventually enhance the light-harvesting capability. As a result, submicrometer-sized mesoporous spheres were considered to be a promising material for dye or QD-sensitized solar cells in view of their high surface area and abundant mesopores. Zhang *et al.* employed submicrometer-sized ZnO aggregates in the preparation of the working electrodes for DSCs and achieved a much improved efficiency (5.4%) than that for ZnO nanocrystals (2.4%).[41,42] A similar result was also obtained for submicrometer-sized TiO_2 beads based DSCs, with a higher overall power conversion efficiency of 7.20% than the cells made from Degussa P25 electrodes (5.66%).[43] The large beads have also been effectively employed as scattering centers or upper scattering layers for the photoanode films to enhance light harvesting by utilizing optical enhancement effects.[44,45] Compared to the extensive research of the beads on DSCs, there is little systematic and in-depth study on such beads for application in QDSCs and there exist some obvious differences between the two types of solar cells. For example, it may be easier for dye molecules to penetrate into the innermost part of the beads to form full coverage than QDs. Earlier work also revealed that anatase TiO_2 with an exposed (101) facet may achieve the most successful dye adsorption,[30] which may not be the case for QDs. Shu *et al.* reported a power conversion efficiency of 3.67% based on mesoscopic nitrogen-doped TiO_2 spheres for QDSCs,[46] while further systematic study was still expected to improve the cell performance of such mesoporous TiO_2 beads for QDSC application.

This paper reports the synthesis of mesoporous TiO_2 beads *via* a facile combination of precipitation and solvothermal processes and the use of the mesoporous TiO_2 beads for the photoanode film of CdS/CdSe co-sensitized solar cells. The mesoporous beads consist of numerous nanocrystallites. These submicrometer-sized beads function as efficient light scatterers, while the nano-sized crystallites in the beads provide the films with a desired mesoporous structure offering a large internal surface area, which allows high QD loading. The combination of strong light scattering and large surface area makes the mesoporous TiO_2 beads superior candidates for QDSC application. Through the ammonia treatment of these beads during the solvothermal process, a power conversion efficiency up to 4.05% has been obtained based on a CdS/CdSe QDs co-sensitized solar cell.

2. Experimental

2.1 Synthesis of mesoporous TiO_2 beads

Mesoporous TiO_2 beads were prepared from a combined precipitation and solvothermal process.[43,47] Firstly, amorphous precursor beads were prepared *via* a precipitation process in the presence of hexadecylamine (HAD, 90%, Sigma-Aldrich) as a structure-directing agent and KCl to control the monodispersity of the precursor beads by adjusting the ionic strength of the solution.[47] 5.296 g HAD was dissolved in 800 mL ethanol, followed by the addition of 3.20 mL KCl aqueous solution (0.1 M). To this solution, 17.6 mL titanium (IV) isopropoxide (TIP, 97%, Sigma-Aldrich) was added under vigorous stirring at ambient temperature. The resulting white TiO_2 suspension was kept static at the same temperature for 18 h, and then centrifuged. The beads were washed with ethanol three times and dried in air at room temperature. Secondly, to prepare mesoporous TiO_2 beads with a highly crystalline framework, a solvothermal treatment of the air-dried precursor beads was performed. Specifically, 0.96 g of the amorphous precursor beads was dispersed in a mixture of 12 mL ethanol and 6 mL deionized water with 0, 0.5, 1 and 2 mL of 25% ammonia solution. Then the resulting mixtures were sealed within a 30 mL autoclave and heated at 160 °C for 16 h. After centrifugation and ethanol washing, the air-dried powders were calcined at 500 °C for 2 h in air to remove organic residuals, resulting in the formation of mesoporous TiO_2 beads.

2.2 Preparation of TiO_2 bead films

To prepare the QDSC photoanode films, 0.5 g of solvothermally treated TiO_2 beads mixed with 0.25 g of ethylcellulose and 1.75 g of α-terpineol were first dispersed into 5.0 mL ethanol, and then sonicated for 30 min to form a slurry after removing ethanol under stirring. Finally, the doctor blade technique was employed to coat the resulting slurry on FTO glass substrates, followed by sintering at 500 °C for 30 min in air with a heating rate of 5 °C min^{-1}. The thickness of the TiO_2 film, measured from the cross-sectional image of SEM, was ~17 μm. The active area of the TiO_2 films was approximately 0.36 cm^2 (0.6 cm × 0.6 cm square).

2.3 Fabrication of CdS/CdSe QDs co-sensitized photoanodes

For the growth of CdS QDs, the TiO_2 films were first immersed into 0.1 M cadmium acetate ($Cd(CH_3COO)_2$) methanol solution for 1 min, rinsed with methanol and dried in air. Successively, the films were dipped into 0.1 M sodium sulfide (Na_2S) solution mixed with water and methanol (1/1, volume ratio) for another 1 min to allow S^{2-} to react with the pre-adsorbed Cd^{2+}, leading to the formation of CdS QDs. Then, the electrodes were again rinsed with methanol and dried. The two-step dipping

procedure is termed as one successive ionic layer absorption and reaction (SILAR) cycle. Four cycles were employed to obtain a suitable amount of CdS QDs on the films. The CdS QDs layer serves as a seeding layer facilitating the subsequent CdSe QDs growth. As for the CdSe QDs deposited on the CdS-coated TiO_2 films, a chemical bath deposition (CBD) method was employed. Briefly, 0.1 M sodium selenosulphate (Na_2SeSO_3) aqueous solution, 0.1 M $Cd(CH_3COO)_2$ aqueous solution, and 0.2 M trisodium salt of nitrilotriacetic acid ($N(CH_2COONa)_3$) solution were mixed together with a volume ratio of 1 : 1 : 1. Then the CdS-coated TiO_2 films were vertically immersed into the solution for the deposition of a CdSe layer under dark conditions at 24 °C for 3 h. After the deposition of CdSe, a zinc sulfide (ZnS) passivation layer was deposited by dipping alternatively into 0.1 M zinc acetate ($Zn(CH_3COO)_2$) and 0.1 M Na_2S solutions for 1 min per dip with two SILAR cycles. The deposition of ZnS is to improve the stability of the photoanodes.

2.4 Preparation of the electrolyte and counter electrodes

The electrolyte employed in this study was composed of 1 M S and 1 M Na_2S in deionized water. The counter electrode was a Cu_2S film fabricated on a brass foil. The preparation process of the Cu_2S electrode can be described as follows:[9] brass foil was immersed into 37% hydrochloric acid (HCl) solution at about 70 °C for 30 min, then rinsed with water and dried in air. After that, the etched brass foil was dipped into 1 M S and 1 M Na_2S aqueous solution (the electrolyte) for about 5 min, resulting in a black Cu_2S layer forming on the foil. The solar cells were prepared by sandwiching a Cu_2S counter electrode and a QD-sensitized photoanode using a scotch tape spacer (~50 μm in thickness) and permeating with the polysulfide electrolyte.

2.5 Characterization of materials and QDSCs

The morphology of the samples was characterized using a scanning electron microscope (SEM, JSM-7000) equipped with an energy dispersive X-ray (EDX) spectrometer to analyze the element contents, and a transmission electron microscope (TEM, Tecnai G2 F20). X-ray diffraction (Bruker F8 Focus Powder XRD with Cu Kα radiation) was used to verify the crystal phase and estimate the crystal size of the mesoporous TiO_2 beads. The diffractometer was set at 40 kV working voltage and 40 mA tube current, scanned from 20 to 80° at a rate of 0.02° s^{-1}. Nitrogen adsorption–desorption isotherms were measured using a Quantachrome NOVA 4200e system, with samples degassed at 250 °C overnight under vacuum before tests. The multi-point Brunauer–Emmett–Teller (BET) method was used to calculate the specific surface area. The pore size distributions of the samples were derived from the desorption branches of the isotherms based on the Barett–Joyner–Halenda (BJH) model. A thermal scientific UV-Vis-NIR spectrophotometer (Evolution 300 PC) fitted with an integrating sphere accessory was employed for the analysis of the optical absorption and reflectance properties of the TiO_2 bead films. The films were fabricated on FTO glass substrates with an approximate identical thickness for all the samples. A blank glass slide was used as a reference to eliminate the influence of the glass substrate on the optical absorption. The photovoltaic properties were measured using an HP 4155A programmable semiconductor parameter analyzer under AM 1.5 simulated sunlight with a power density of 100 mW cm^{-2}. Electrochemical impedance spectroscopy (EIS) was carried out using a Solartron 1287A coupled with a Solartron 1260 FRA/impedance analyzer to investigate the electronic and ionic processes in QDSCs.

3. Results and discussion

SEM images of the as-prepared precursor material and the calcined mesoporous TiO_2 beads prepared *via* the solvothermal process with different amounts of ammonia solution are shown in Fig. 1a–f. The precursor beads possess a quite smooth surface with the diameter in the range of ~1000 ± 100 nm, exhibiting a little polydispersity, while a relatively rough surface with a little

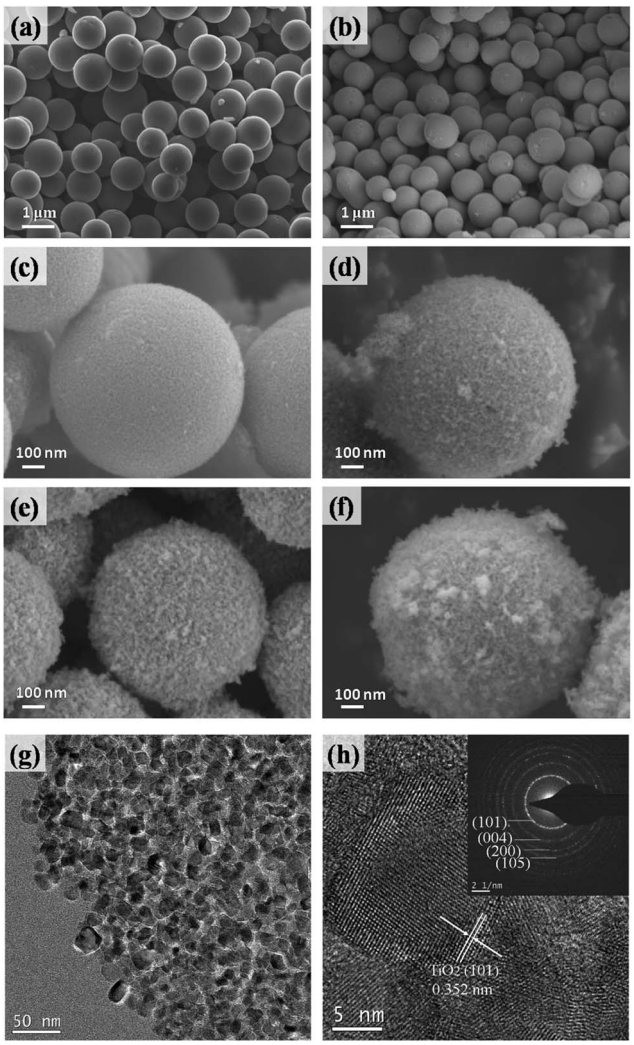

Fig. 1 SEM images of the as-prepared (a) precursor material and calcined mesoporous TiO_2 beads obtained after a solvothermal process with (b and c) 0 mL, (d) 0.5 mL, (e) 1 mL and (f) 2 mL ammonia solution; (g) TEM and (h) HRTEM images of the ultramicrotomed sample of the calcined mesoporous TiO_2 beads without ammonia treatment during the solvothermal process. The inset of (h) shows the SAED pattern of TiO_2 beads.

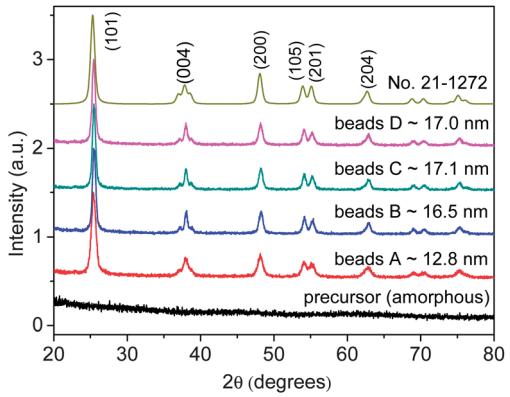

Fig. 2 XRD patterns of the precursor material and the calcined mesoporous TiO_2 beads A, B, C and D. The top is the standard profile of anatase TiO_2 (JCPDS card no. 21-1272). The nanocrystallite sizes of the beads, as labeled in the figure, were estimated using the Scherrer equation.

shrinkage in the bead diameter (~850 ± 80 nm for the mesoporous beads) was produced after the solvothermal treatment followed by calcination. The beads prepared with the addition of 0, 0.5, 1 and 2 mL ammonia to a mixture of 12 mL ethanol and 6 mL deionized water during the solvothermal treatment are denoted as beads A, B, C and D, respectively. A more pronounced rough surface and enlarged pores were obtained with the increasing amount of ammonia. This indicates that ammonia etches the precursor beads, and a high concentration of ammonia results in large pores. The TEM image (Fig. 1g) of the calcined beads without ammonia treatment during the solvothermal process displays individual nanocrystallites with an average diameter of ~13 nm and abundant intercrystalline pores throughout the beads. The HRTEM (high-resolution TEM) image of Fig. 1h allows the identification of the lattice fringes with a *d*-spacing of 0.352 nm correlated with the (101) planes of anatase TiO_2 and the distinct SAED pattern shown in the inset also confirmed the crystalline anatase phase of the beads.

Fig. 2 gives the XRD patterns of the precursor material and the calcined TiO_2 beads A, B, C and D after solvothermal treatment. The precursor material was amorphous as expected. After the solvothermal and calcination treatment, XRD patterns of these beads showed well-resolved diffraction peaks corresponding to anatase TiO_2 (JCPDS card no. 21-1272). Moreover, the diffraction peaks for beads B, C and D were sharper than that for bead A, and the (103), (112), (105) and (201) reflections were better resolved. The nanocrystallite sizes for these beads were estimated using the Scherrer equation based on the full width at half maximum (FWHM) of the strongest (101) peak,[48] as labeled in Fig. 2. The average size of TiO_2 nanocrystallites increased from ~13 nm to ~17 nm with the ammonia treatment, and this implies that the presence of ammonia promoted the crystal growth. The crystal size of beads was consistent with what is revealed in the TEM image in Fig. 1g.

The surface areas and pore size distributions of the precursor material and the calcined mesoporous TiO_2 beads were characterized using nitrogen sorption isotherms and the results are shown in Fig. 3a and b. As summarized in Table 1, a very small surface area of 2.64 $m^2 g^{-1}$ for the precursor material indicated a dense structure of the precursor beads, which was in the amorphous form according to XRD characterization. For solid spheres with a diameter of ~1000 nm and smooth surface, the specific surface area would be ~0.71 $m^2 g^{-1}$, when assuming that the material possesses the density of TiO_2 (4.23 g cm^{-3}). Although the density of the amorphous precursor material would be a little lower than that of crystalline TiO_2, the discrepancy between the measured surface area and the calculated one suggests that the precursor beads may not be completely dense, and/or the surface may not be smooth. After the solvothermal and calcination treatment, the beads became more porous and presented relatively large pores. Type IV isotherms with a sharp capillary condensation step at relative

Table 1 BET results of the precursor material and calcined mesoporous TiO_2 beads

Sample	Surface area ($m^2 g^{-1}$)	Pore volume ($cm^2 g^{-1}$)	Pore size (nm)
Precursor	2.64	—	—
Beads A	104.5	0.286	11.5
Beads B	87.0	0.310	16.3
Beads C	86.6	0.376	21.0
Beads D	77.9	0.388	20.9

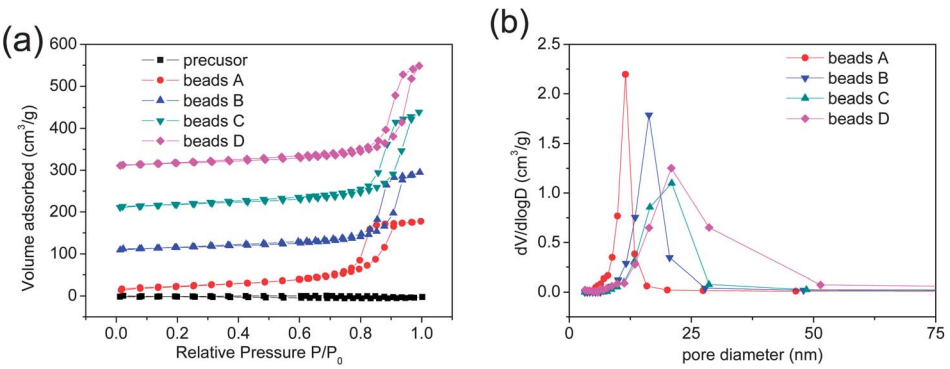

Fig. 3 (a) Nitrogen sorption isotherms and (b) the corresponding pore diameter distributions of the precursor material and calcined mesoporous TiO_2 beads A, B, C and D. The isotherms of samples B, C and D are shifted by 100, 200 and 300 $cm^3 g^{-1}$, respectively.

pressures P/P_0 = 0.8–0.9 and H1 type hysteresis loops were observed for beads A, B, C and D.[49] Beads A exhibited the largest surface area of 104.5 m^2 g^{-1} and a pore size distribution centered at 11.5 nm. Admixing ammonia solution led to an enlargement in both pore size and pore volume, which gradually increased with the increasing amount of ammonia, as what was observed for beads B, C, and D. Such a result is in good agreement with SEM images that the ammonia etching results in large pores. The pore size reached ~20 nm for beads C and D from 11.5 nm of beads A. A corresponding decrease in the surface area from 104.5 to 87.0, 86.6 and 77.9 m^2 g^{-1} was also observed with the increasing amount of ammonia, due to the increased pore size and nanocrystallite size. These are consistent with the results reported by Chen *et al.*[43] Unlike large oxide particles, the mesoporous beads are made of packed nanocrystallites, and thus possess a high specific surface area, which would benefit the loading of dye molecules or QDs in the case of solar cell application. In addition, the large pores in the beads would favor an easy penetration of QDs into the inner pores of mesoporous beads, while the decreased surface area plays a negative role in high QDs loading.

Working electrode films were prepared using these mesoporous TiO_2 beads for QDSC application. Fig. 4a and b give the SEM images of the TiO_2 film surfaces before and after CdS/CdSe QD sensitization, respectively. As shown, after QD sensitization, the film surface became a little blurry due to the adsorption of QDs compared to the films prior to sensitization. EDX images shown in the insets of Fig. 4 clearly demonstrated the presence of CdS and CdSe. The pure TiO_2 film only exhibited two typical energy dispersion peaks for Ti and O, while for the film sensitized by CdS/CdSe QDs, three additional strong peaks corresponding to Se, S and Cd were obtained, which confirmed the deposition of CdS and CdSe QDs onto the mesoporous TiO_2 bead film. The photoanode films consisting of submicrometer-sized mesoporous TiO_2 beads can significantly enhance the photon capturing capability due to the presence of light scattering. As illustrated in the schematic of Fig. 4e, the diffuse reflection significantly extends the traveling distance of light within the photoanode film and thus increases the opportunities for incident photons to be captured by the sensitizer. A photon-localization effect may also occur on these films when the light scattering is confined in closed loops.

TEM images as shown in Fig. 4d further corroborated the penetration of QDs into the mesoporous beads. Compared to the image (Fig. 4c) of pure TiO_2 beads which clearly revealed the regular-shaped individual crystals with a clean boundary and size in the beads, the image for TiO_2 beads after QDs were adsorbed exhibited a layer of small particles homogeneously covered on the surface of TiO_2, making the boundary of TiO_2 nanocrystallites obscure and the individual crystals difficult to distinguish. Such small nanoparticles are presumably the as-grown CdS/CdSe QDs, adsorbing on the TiO_2 to form a thin coating layer.[9,10] A profile drawing of mesoporous TiO_2 beads with CdS/CdSe QDs loaded is shown in Fig. 4e.

Fig. 5 presents *J–V* curves for CdS/CdSe QDs co-sensitized solar cells using the photoanodes prepared from mesoporous beads A, B, C, and D, respectively. The open circuit voltage (V_{oc}), short circuit current density (J_{sc}), fill factor (FF), and overall power conversion efficiencies (η) of those QDSCs are summarized in Table 2. It is evident that the ammonia treatment

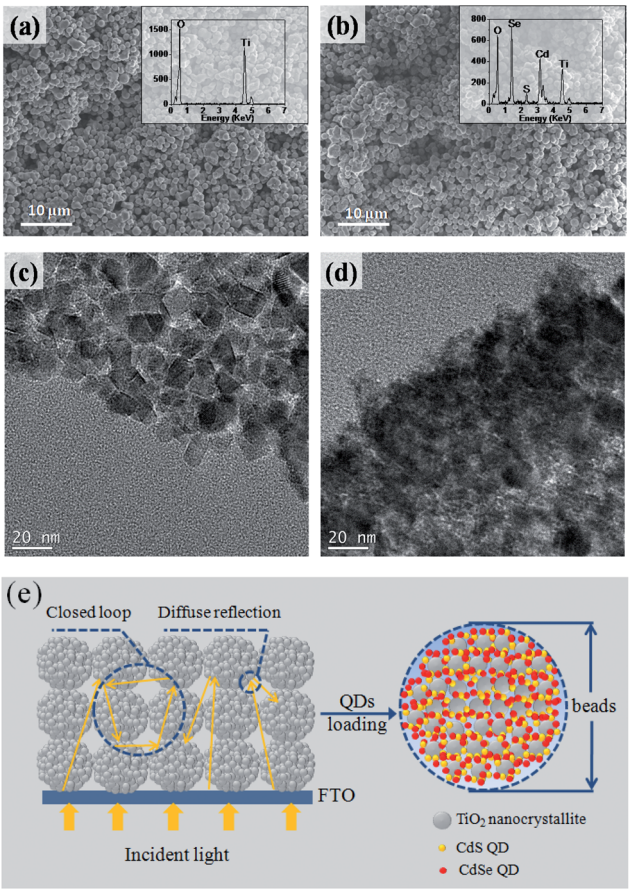

Fig. 4 SEM images of the mesoporous TiO_2 bead film surfaces (a) before and (b) after CdS/CdSe QD sensitization (the insets show the corresponding EDX images), TEM images of TiO_2 beads (c) before and (d) after QDs are adsorbed, and (e) schematic of the light scattering effect and photon localization within a film consisting of mesoporous TiO_2 beads and the profile drawing of mesoporous TiO_2 beads with CdS/CdSe QDs loaded.

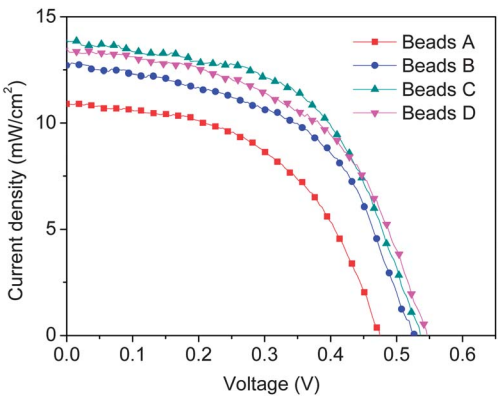

Fig. 5 *J–V* curves for CdS/CdSe QDs co-sensitized solar cells using the photoanodes prepared by mesoporous TiO_2 beads A, B, C and D, measured under the illumination of one sun (AM 1.5, 100 mW cm^{-2}).

Table 2 Photovoltaic properties of CdS/CdSe QDs co-sensitized solar cells using the photoanodes prepared by mesoporous TiO_2 beads A, B, C and D, measured under the illumination of one sun (AM 1.5, 100 mW cm^{-2})

Electrodes	V_{oc} (V)	J_{sc} (mA cm^{-2})	FF	η (%)
Beads A	0.48	10.90	0.51	2.63
Beads B	0.53	12.70	0.53	3.53
Beads C	0.54	13.89	0.54	4.05
Beads D	0.55	13.46	0.52	3.84

during the solvothermal process resulted in the increase of both J_{sc} and V_{oc}, and thus led to enhanced performance. The TiO_2 electrode made of beads A showed a J_{sc} of 10.90 mA cm^{-2}, V_{oc} of 0.48 V and η of 2.63%, whereas the electrode made of beads C achieved a J_{sc} of 13.89 mA cm^{-2}, V_{oc} of 0.54 V and η of 4.05%, indicating an improvement of 54% in the power conversion efficiency compared to the beads A electrode. The beads D photoanode exhibited a little drop in the cell performance. The increase of J_{sc} is mainly attributed to more effective generation of photoexcited electrons, while the improvement of V_{oc} and FF can be explained by the reduced charge recombination for the TiO_2 beads treated with ammonia; more ammonia treatment yields larger pores, benefiting the penetration of QDs and thus causing higher coverage of the TiO_2 surface.[9,10,30] The specific reasons will be further discussed later.

The amount of QDs loaded on the TiO_2 electrode affects the cell current density of QDSCs, which is similar to DSCs. Optical absorbance was employed to measure the amount of QDs adsorbed on TiO_2 electrodes. In order to minimize the influence of the light scattering effect involved in the measurements, very thin films (~7 μm in thickness) were prepared for the study of optical absorbance. Fig. 6 illustrates the optical absorbance spectra of CdS/CdSe co-sensitized photoanode films prepared from beads A, B, C and D. All the films exhibited absorption over a wide wavelength range (from 300 to 630 nm), attributing to the CdS/CdSe QD adsorption. The absorbance of the films increased from beads A to B, to C and to D, which followed the trend of increased pore size and pore volume but a decreased specific surface area. Assuming the TiO_2 surfaces were the same for the QDs deposition in all samples, a large surface area would accommodate more QDs. However, considering the pore size and the tortuous nature of the pores, the precursor solutions may have difficulty in accessing the inner pores when the pores are small, and thus some of the surface area may not be accessible. This might explain why beads A with the largest surface area and smallest pores exhibited the weakest absorbance among the four samples. In contrast, large pores created by the ammonia treatment during the solvothermal process would provide easy pathways for the precursor solution to penetrate into the inner pores, and thus increase the QD loading. Although a decreased surface area would hamper the QDs loading, pore size and pore volume seem to have more pronounced impacts on QDs loading in the present investigation. The increased QD loading contributed to the increase of light absorption and thus current density.

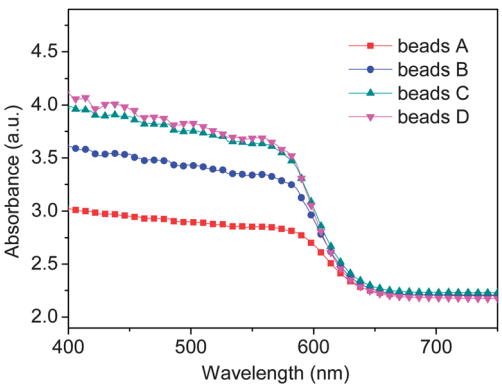

Fig. 6 UV-Vis spectra of CdS/CdSe QDs co-sensitized photoanode films prepared by beads A, B, C and D.

The size of CdSe QDs can be estimated using the UV-Vis absorption spectrum based on the following equation:[50,51]

$$\Delta E = E_1 - E_g = \frac{h^2}{8r^2}\left(\frac{1}{m_e} + \frac{1}{m_h}\right) \quad (1)$$

where ΔE is the band gap shift, E_1 is the band gap of CdSe QDs, E_g is the band gap of the bulk materials (1.74 eV for bulk CdSe), r is the radius of QDs, and m_e and m_h are the effective masses of electrons and holes, respectively. As all the absorption edges of four spectra locate at around 630 nm, the band gap of as grown CdSe QDs is calculated to be 1.97 eV, and thus $\Delta E = 0.23$ eV. Moreover, for the CdSe material, $m_e = 0.13m_0$ and $m_h = 0.44m_0$ ($m_0 = 9.11 \times 10^{-31}$ kg). Eventually, the radius of CdSe QDs is estimated to be ~4.04 nm, which is consistent with the TEM observation as shown in Fig. 4.

The photoanode films made from mesoporous TiO_2 beads have high diffuse reflection capabilities due to the bead size comparable to the wavelength of visible light, as demonstrated in Fig. 4e. An increase in the light scattering ability of the photoanode is very important for enhancing the light harvesting efficiency, and thus boosting the J_{sc} of QDSCs. The light scattering ability can be evaluated by recording the diffuse reflectance spectra of the TiO_2 films. Fig. 7a and b give the diffuse reflectance spectra of the TiO_2 films prepared from various mesoporous beads before and after CdS/CdSe QD sensitization. The diffuse reflectance results demonstrated quite high light reflectance for the films in the visible and near-infrared regions, and a gradual decrease of light reflectance from beads A to B, C and D, either before or after QD sensitization. The remarkable drop for the diffuse reflectance spectra over the wavelength ranging from 400 to 650 nm mainly resulted from the strong light absorption by CdS/CdSe QDs. Such a decrease of the scattering effect might be due to the destruction of perfect mesoporous spheres. As presented above, the ammonia treatment brought about larger pore sizes and more pronounced rough surfaces, which decreased the scattering capability of the beadswhile it increased on approaching the individual nanoparticles. This explains why beads D with the most remarkable surface roughness exhibited the lowest diffuse reflectance. Of course, there were still striking differences between individual nanoparticles and beads in our case. All of the as prepared beads A, B, C and D possessed higher scattering

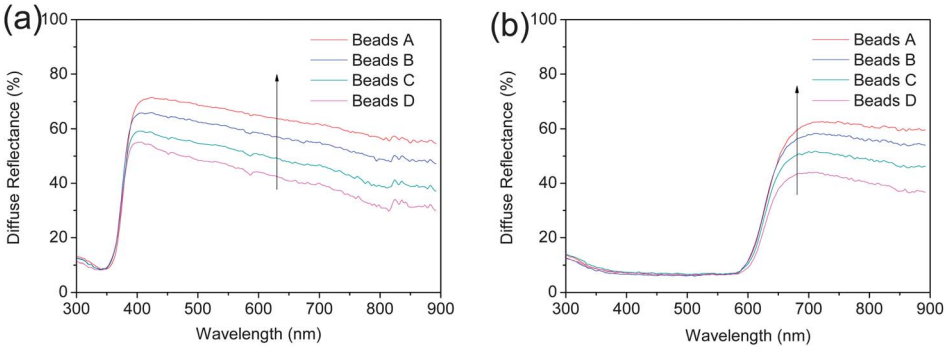

Fig. 7 Diffuse reflectance spectra of the TiO_2 films prepared from mesoporous beads A, B, C and D (a) before and (b) after CdS/CdSe QD sensitization.

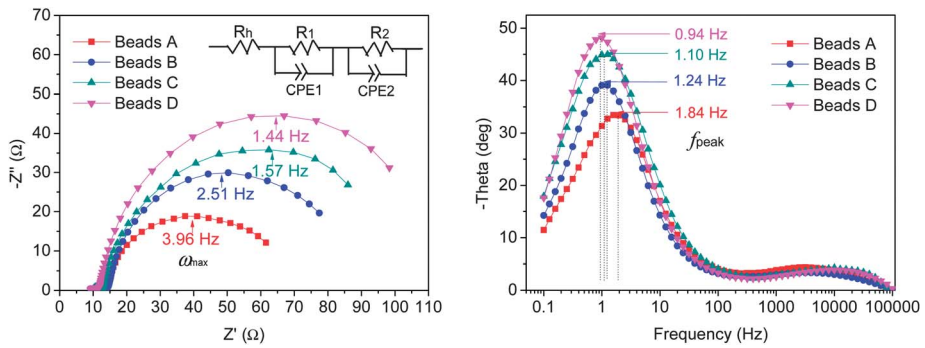

Fig. 8 (a) Nyquist plots and (b) Bode plots of EIS spectra recorded under dark conditions at an applied forward bias of −0.6 V for QDSCs with the photoanodes prepared from mesoporous beads A, B, C and D. The inset displays the corresponding equivalent circuit.

effect than individual nanocrystals. Evidently, the decrease of the diffuse reflection capabilities for the beads treated with the increasing amount of ammonia would unavoidably lower the effective photon captured and thus lead to undesirable decrease of the achieved photocurrent.

To evaluate the resistance distributions and charge recombination processes for various beads, electrochemical impedance spectroscopy (EIS) measurements were conducted. Fig. 8 shows the impedance spectra of QDSCs employing various TiO_2 beads as the photoanodes measured under forward bias (−0.6 V) under dark conditions. As shown in Fig. 8a, the Nyquist plots exhibited two semicircles which corresponded to the electron ejection at the counter electrode/electrolyte interface and transport in the electrolyte at high frequencies (R_1, smaller semicircle), and the electron transfer at the TiO_2/QDs/electrolyte interface and transport in the TiO_2 film (R_2, bigger semicircle), respectively.[52] Summarized in Table 3 are the fitting results of the charge transfer resistance. Apparently, R_2 increased from beads A to B, C and D, which suggested the reduced interfacial recombination.[9,10,46] This is closely associated with the structural features of various beads. The increase of R_2 is mainly attributed to the reduction of the contact area of TiO_2 with the electrolyte, because the poor QD loading for beads A causes the direct exposure of TiO_2 to the electrolyte. In contrast, large pores may benefit the penetration of QDs into mesoporous beads, result in high coverage of the TiO_2 surface, and moreover facilitate the permeation of the electrolyte. Thus,

Table 3 Electrochemical impedance results (charge transfer resistance and electron lifetime) of QDSCs with the photoanodes prepared from mesoporous beads

Photoanodes	R_1 (Ω)	R_2 (Ω)	τ_n (ms)
Beads A	2.3	52.6	87
Beads B	2.3	71.9	128
Beads C	2.2	84.7	145
Beads D	2.0	98.5	169

the charge recombination between the injected electrons and the oxidized ions (S_n^{2-}) in the electrolyte can be suppressed. The analysis coincided with the photovoltaic results which demonstrated the increase of V_{oc} and FF for beads B, C, and D due to the decreased electron recombination, compared to beads A without the ammonia treatment. Fig. 8b gives the Bode plots of the impedance spectra of QDSCs. The electron lifetimes (τ_n) in the photoanodes of various TiO_2 beads can be evaluated by the peak frequency at the minimum phase angle (ω_{peak}) in the Bode plots based on the following relationship:[53,54]

$$\tau_n = \frac{1}{\omega_{peak}} = \frac{1}{2\pi f_{peak}} \quad (2)$$

The values of f_{peak} are shown in the Bode plots of Fig. 8b and exhibit a gradual decrease from beads A to B, C and D. The calculated values of electron lifetimes are listed in Table 3. The

results indicated that the electron lifetime of the device was prolonged from 87 ms to 169 ms due to the treatment with higher concentration ammonia from beads A to D. The long-lived charge carrier implied a low charge recombination, so as to improve V_{oc} and FF of QDSCs.

Furthermore, for DSCs, it is generally accepted that a decrease in the frequency at the maximum imaginary resistance of the second semicircle (ω_{max}) in the Nyquist plot is correlated with an increase in V_{oc}, which is due to the retarded back-reaction of injected electron transfer at the TiO_2/QDs/electrolyte interface under open circuit conditions and illumination. The V_{oc} of a DSC can be expressed by the following equation:[55,56]

$$V_{oc} = \frac{RT}{\beta F}\ln\left(\frac{AI}{n_0 k_b [I_3^-] + n_0 k_r [D^+]}\right) \quad (3)$$

where R is the molar gas constant, T is the temperature, F is the Faraday constant, β is the reaction order for I_3^- and electrons, A is the electrode area, I is the incident photon flux, n_0 is the concentration of accessible electronic states in the conduction band, and k_b and k_r are the kinetic constants of the back-reaction of the injected electrons with triiodide and the recombination of these electrons with oxidized dyes (D^+), respectively. For QDSCs, the redox couple is S^{2-}/S_n^{2-} instead of I^-/I_3^-. Considering that ω_{max} is the same as the back-reaction constant (k_b),[55,57] and that S_n^{2-} in the electrolyte is constant under our experimental conditions, V_{oc} will depend logarithmically on $1/\omega_{max}$ as the loss term $n_0 k_r[D^+]$ can be neglected.[55,56] As demonstrated in Fig. 8a, the QDSC device exhibited a gradual decrease of ω_{max} from beads A to B, C and D. Therefore, according to eqn (3), the value of V_{oc} of QDSC could increase as the beads are treated with the higher concentration of ammonia, which was consistent with the results obtained from J–V curves.

To summarize, the most significant advantages of the mesoporous TiO_2 beads for solar cell application are their high surface area, which allows high QD loading and their superior light scattering properties, which enhance the light-harvesting capability of the photoanodes. Through the ammonia treatment during the solvothermal process, the performance of QDSCs can be significantly improved due to the increased QD loading and reduced charge recombination. However, large voids existing between the submicrometer-sized mesoporous beads will unavoidably result in a loss of internal surface area of the photoanode film and increase the recombination rate of photogenerated carriers due to an incompact connectivity between the beads.[45,58] The combined use of mesoporous TiO_2 beads and TiO_2 nanoparticles (*e.g.*, commercial P25 nanoparticle) not only opens up a room to further increase the internal surface area of the photoanode film, but also offers the opportunity to achieve high light scattering and weak charge recombination. Therefore, efforts are underway to study the use of the mesoporous TiO_2 beads as the scattering centers and upper scattering layer in the photoanode film combined with the P25 TiO_2 nanoparticles for QDSC application and better cell performances are expected to be achieved.

4. Conclusions

Mesoporous anatase TiO_2 beads have been prepared through a combined precipitation and solvothermal process. The sub-micrometer-sized mesoporous TiO_2 beads with high specific surface areas are ideal for the QDSC application due to the dual functions of high QD loading and strong light scattering. The addition of ammonia during the solvothermal treatment process has several impacts on the cell performance: (a) it creates large pores favoring high QD loading and conformal QD coverage, which in turn (b) reduces the charge recombination of photogenerated carriers and prolongs the electron lifetime, so as to enhance the V_{oc} and FF; however, excessive ammonia would (c) lead to a much decreased specific surface area which lowers the QD loading, and (d) weakens the light scattering effect and thus reduces the light harvesting within the photoanodes. The successful balance of the competition between the positive impacts (a and b) and negative impacts (c and d) has resulted in an overall power conversion efficiency up to 4.05% for CdS/CdSe QDs co-sensitized solar cells by employing the photoanode made of mesoporous TiO_2 beads.

Acknowledgements

This work was supported in part by the National Science Foundation (DMR 1035196), the University of Washington TGIF grant, and the Royalty Research Fund (RRF) from the Office of Research at the University of Washington. Ru Zhou would also like to acknowledge the fellowship from the China Scholarship Council.

References

1 A. Zaban, O. I. Mićić, B. A. Gregg and A. J. Nozik, *Langmuir*, 1998, **14**, 3153–3156.
2 P. K. Santra and P. V. Kamat, *J. Am. Chem. Soc.*, 2012, **134**, 2508–2511.
3 M. A. Hossain, J. R. Jennings, Z. Y. Koh and Q. Wang, *ACS Nano*, 2011, **5**, 3172–3181.
4 J. Ryu, S. H. Lee, D. H. Nam and C. B. Park, *Adv. Mater.*, 2011, **23**, 1883–1888.
5 T. Sugaya, O. Numakami, R. Oshima, S. Furue, H. Komaki, T. Amano, K. Matsubara, Y. Okano and S. Niki, *Energy Environ. Sci.*, 2012, **5**, 6233–6237.
6 P. V. Kamat, *J. Phys. Chem. C*, 2008, **112**, 18737–18753.
7 V. Gonzalez-Pedro, X. Xu, I. Mora-Sero and J. Bisquert, *ACS Nano*, 2010, **4**, 5783–5790.
8 G. Zhu, L. Pan, T. Xu and Z. Sun, *ACS Appl. Mater. Interfaces*, 2011, **3**, 3146–3151.
9 J. J. Tian, Q. F. Zhang, E. Uchaker, Z. Q. Liang, R. Gao, X. H. Qu, S. G. Zhang and G. Z. Cao, *J. Mater. Chem. A*, 2013, **1**, 6770–6775.
10 J. J. Tian, Q. F. Zhang, L. L. Zhang, R. Gao, L. F. Shen, S. G. Zhang, X. H. Qu and G. Z. Cao, *Nanoscale*, 2013, **5**, 936–943.
11 O. E. Semonin, J. M. Luther, S. Choi, H.-Y. Chen, J. B. Gao, A. J. Nozik and M. C. Beard, *Science*, 2011, **334**, 1530–1533.

12 M. C. Hanna and A. J. Nozik, *J. Appl. Phys.*, 2006, **100**, 074510.
13 W. Shockley and H. J. Queisser, *J. Appl. Phys.*, 1961, **32**, 510–519.
14 S. C. Lin, Y. L. Lee, C. H. Chang, Y. J. Shen and Y. M. Yang, *Appl. Phys. Lett.*, 2007, **90**, 143517.
15 Y. Tak, S. J. Hong, J. S. Lee and K. Yong, *J. Mater. Chem.*, 2009, **19**, 5945–5951.
16 J. Kim, H. Choi, C. Nahm, J. Moon, C. Kim, S. Nam, D. R. Jung and B. Park, *J. Power Sources*, 2011, **196**, 10526–10531.
17 I. Robel, V. Subramanian, M. Kuno and P. V. Kamat, *J. Am. Chem. Soc.*, 2006, **128**, 2385–2393.
18 M. Samadpour, S. Giménez, P. P. Boix, Q. Shen, M. E. Calvo, N. Taghavinia, A. I. zad, T. Toyoda, H. Míguez and I. Mora-Seró, *Electrochim. Acta*, 2012, **75**, 139–147.
19 Z. Yang and H.-T. Chang, *Sol. Energy Mater. Sol. Cells*, 2010, **94**, 2046–2051.
20 M. Samadpour, A. I. zad, N. Taghavinia and M. Molaei, *J. Phys. D: Appl. Phys.*, 2011, **44**, 045103.
21 A. Braga, S. Giménez, I. Concina, A. Vomiero and I. Mora-Sero, *J. Phys. Chem. Lett.*, 2011, **2**, 454–460.
22 R. Plass, S. Pelet, J. Krueger, M. Grätzel and U. Bach, *J. Phys. Chem. B*, 2002, **106**, 7578–7580.
23 A. Tubtimtae, K. L. Wu, H. Y. Tung, M. W. Lee and G. J. Wang, *Electrochem. Commun.*, 2010, **12**, 1158–1160.
24 C. Chen, Y. Xie, G. Ali, S. H. Yoo and S. O. Cho, *Nanoscale Res. Lett.*, 2011, **6**, 462.
25 Y. L. Lee and Y. S. Lo, *Adv. Funct. Mater.*, 2009, **19**, 604–609.
26 J. J. Tian, R. Gao, Q. F. Zhang, S. G. Zhang, Y. W. Li, J. L. Lan, X. H. Qu and G. Z. Cao, *J. Phys. Chem. C*, 2012, **116**, 18655–18662.
27 M. A. Hossain, J. R. Jennings, C. Shen, J. H. Pan, Z. Y. Koh, N. Mathews and Q. Wang, *J. Mater. Chem.*, 2012, **22**, 16235–16242.
28 A. Yella, H. W. Lee, H. N. Tsao, C. Y. Yi, A. K. Chandiran, M. K. Nazeeruddin, E. W. G. Diau, C. Y. Yeh, S. M. Zakeeruddin and M. Grätzel, *Science*, 2011, **334**, 629–634.
29 M. Grätzel, *Inorg. Chem.*, 2005, **44**, 6841–6851.
30 Q. F. Zhang, K. Park, J. T. Xi, D. Myers and G. Z. Cao, *Adv. Energy Mater.*, 2011, **1**, 988–1001.
31 M. Law, L. E. Greene, J. C. Johnson, R. Saykally and P. D. Yang, *Nat. Mater.*, 2005, **4**, 455–459.
32 M. Paulose, K. Shankar, O. K. Varghese, G. K. Mor and C. A. Grimes, *J. Phys. D: Appl. Phys.*, 2006, **39**, 2498–2503.
33 A. Usami, *Chem. Phys. Lett.*, 1997, **277**, 105–108.
34 J. Ferber and J. Luther, *Sol. Energy Mater. Sol. Cells*, 1998, **54**, 265–275.
35 G. Rothenberger, P. Comte and M. Grätzel, *Sol. Energy Mater. Sol. Cells*, 1999, **58**, 321–336.
36 C. J. Barbe, F. Arendse, P. Comte, M. Jirousek, F. Lenzmann, V. Shklover and M. Grätzel, *J. Am. Ceram. Soc.*, 1997, **80**, 3157–3171.
37 T. P. Chou, Q. F. Zhang, B. Russo, G. E. Fryxell and G. Z. Cao, *J. Phys. Chem. C*, 2007, **111**, 6296–6302.
38 S. Ito, P. Chen, P. Comte, M. K. Nazeeruddin, P. Liska, P. Pechy and M. Grätzel, *Prog. Photovoltaics*, 2007, **15**, 603–612.
39 H. C. van de Hulst, *Light Scattering by Small Particles*, Wiley, New York, 1957.
40 P. E. Wolf and G. Maret, *Phys. Rev. Lett.*, 1985, **55**, 2696.
41 Q. F. Zhang, T. P. Chou, B. Russo, S. A. Jenekhe and G. Z. Cao, *Angew. Chem.*, 2008, **120**, 2436–2440.
42 Q. F. Zhang, T. R. Chou, B. Russo, S. A. Jenekhe and G. Z. Cao, *Adv. Funct. Mater.*, 2008, **18**, 1654–1660.
43 D. H. Chen, F. Z. Huang, Y. B. Cheng and R. A. Caruso, *Adv. Mater.*, 2009, **21**, 2206–2210.
44 F. Z. Huang, D. H. Chen, X. L. Zhang, R. A. Caruso and Y.-B. Cheng, *Adv. Funct. Mater.*, 2010, **20**, 1301–1305.
45 J. T. Xi, Q. F. Zhang, K. Park, Y. M. Sun and G. Z. Cao, *Electrochim. Acta*, 2011, **56**, 1960–1966.
46 T. Shu, P. Xiang, Z. M. Zhou, H. Wang, G. H. Liu, H. W. Han and Y. D. Zhao, *Electrochim. Acta*, 2012, **68**, 166–171.
47 D. H. Chen, L. Cao, F. Z. Huang, P. Imperia, Y.-B. Cheng and R. A. Caruso, *J. Am. Chem. Soc.*, 2010, **132**, 4438–4444.
48 B. D. Cullity, *Elements of X-ray Diffraction*, Addison-Wesley Publishing Company, New York, 2nd edn, 1978, p. 281.
49 S. Lowell, J. E. Shields, M. A. Thomas and M. Thommes, Characterization of Porous Solids and Powders: Surface Area, *Pore Size and Density*, Kluwer, London, 2004.
50 Q. Shen, J. Kobayashi, L. J. Diguna and T. Toyoda, *J. Appl. Phys.*, 2008, **103**, 084304.
51 L. W. Chong, H. T. Chien and Y. L. Lee, *J. Power Sources*, 2010, **195**, 5109–5113.
52 N. Koide, A. Islam, Y. Chiba and L. Y. Han, *J. Photochem. Photobiol., A*, 2006, **182**, 296–305.
53 J. Bisquert, F. Fabregat-Santiago, I. Mora-Seró, G. Garcia-Belmonte and S. Gimenez, *J. Phys. Chem. C*, 2009, **113**, 17278–17290.
54 R. Kern, R. Sastrawan, J. Ferber, R. Stangl and J. Luther, *Electrochim. Acta*, 2002, **47**, 4213–4225.
55 K. Lee, S. W. Park, M. J. Ko, K. Kim and N.-G. Park, *Nat. Mater.*, 2009, **8**, 665–671.
56 Q. Wang, J.-E. Moser and M. Grätzel, *J. Phys. Chem. B*, 2005, **109**, 14945–14953.
57 M. Adachi, M. Sakamoto, J. Jiu, Y. Ogata and S. Isoda, *J. Phys. Chem. B*, 2006, **110**, 13872–13880.
58 Y. J. Kim, M. H. Lee, H. J. Kim, G. Lim, Y. S. Choi, N. G. Park, K. Kim and W. I. Lee, *Adv. Mater.*, 2009, **21**, 3668–3673.